RESEARCH ARTICLE

# Application of multi-window maximum cross-correlation to the mediterranean sea circulation by using MODIS data

**Bartolomeo Doronzo[1,2*], Stefano Taddei[1] and Carlo Brandini[1,2]**

[1] Consorzio LaMMA, Via Madonna del Piano 10, 50019 Sesto Fiorentino, Italy.
[2] Istituto di Biometeorologia IBIMET-CNR, Via Giovanni Caproni 8, 50145 Firenze, Italy.

**Abstract**: In a previous study an improved Maximum Cross-Correlation technique, called Multi-Window Maximum Cross-Correlation (MW-MCC), was proposed, and applied to noise-free synthetic images in order to show its potential and limits in oceanographic applications. In this work, instead, the application of MW-MCC to high resolution MODIS images, and its capability to provide useful and realistic results for ocean currents, is studied.

When applied to real satellite images, the MW-MCC is subject to cloud cover and image quality problems. As a consequence the number of useful MODIS images is greatly reduced. However, for every MODIS image, multiple spectral bands are available, and it is possible to apply the MW-MCC algorithm to the same scene as many times as the number of these bands, increasing the possibility of finding valid current vectors.

Moreover, the comparison among the results from different spectral bands allows to verify both the consistency of the computed current vectors and the validity of using a spectral band as a good tracer for the ocean circulation.

Due to the lack of systematic current measurements in the area considered, it has been not possible to perform an extensive error analysis of the MW-MCC results, although a case study of a comparison between HF radar measurements and MW-MCC data is shown. Moreover, some comparison between numerical ocean model simulations and MW-MCC results are also shown. The coherence of the resulting circulation flow, the high number of current vectors found, the agreement among different spectral bands, and conformity with the currents measured by the HF radars or simulated by hydrodynamic models show the validity of the technique.

**Keywords**: Maximum cross-correlation, surface currents, MODIS dataset analysis.

*Correspondence to: Bartolomeo Doronzo, Istituto di Biometeorologia IBIMET-CNR, Via Giovanni Caproni 8, 50145 Firenze, Italy. Email: b.doronzo@lamma.rete.toscana.it

**Received:** August 30, 2016; **Accepted:** October 29, 2016; **Published Online:** November 30, 2016

**Citation:** Doronzo B, Taddei S and Brandini C, (2017). Application of multi-window maximum cross-correlation to the mediterranean sea circulation by using MODIS data. *Satellite Oceanography and Meteorology*, vol.2(1): 10–25. http://dx.doi.org/10.18063/SOM.2017.01.002.

## 1. Introduction

The potentiality and usefulness of the Maximum Cross-Correlation (MCC) technique for studying the ocean circulation has been widely demonstrated (e.g., Emery *et al*, 1986; Garcia and Robinson, 1989; Kamachi, 1989; Breaker *et al*, 1994; Matthews and Emery, 2009; Doronzo *et al*, 2015). It is one of the fastest and cheapest ways to detect current flows on large oceanic surfaces. The method allows

the circulation to be studied over many hundreds of square kilometres just by using pairs of high-resolution satellite images usually exploited for other purposes, such as the estimation of sea surface temperature (SST). Measurements on such a wide area are very difficult with traditional in-situ instruments, due to logistical difficulties and costs of oceanographic surveys. Another possibility for such large-scale observations is represented by the latest generation terrestrial remote sensing systems, like HF radars, which are now spreading even in the Mediterranean Sea, although they are quite expensive.

Many versions of the MCC technique have been proposed in the literature (Kamachi, 1989; Barton 2002; Bowen *et al*, 2002; Zavialov *et al*, 2002; Emery *et al*, 2003; Notarstefano *et al*, 2008). A Multi-Window Maximum Cross-Correlation (MW-MCC) has recently been developed, and tested on mainly synthetic imagery obtained with a regional high resolution ROMS model (Doronzo *et al*, 2015). A systematic analysis has been done on a large noise-free synthetic image dataset in order to demonstrate the potentialities and limits of the algorithm. MW-MCC differs from previous MCC algorithms because it is not based on a single template window, but on some distinct windows of different sizes. It has been shown that this implementation leads to a more robust and accurate estimation of current vectors.

This paper describes, for the first time, an extensive application of MW-MCC to high resolution MODIS images.

The performance of the MW-MCC method, when applied to real satellite images rather than synthetic ones, is strongly affected by cloud cover and image quality (e.g., noise, striping, and georeferencing effects).

The most significant problem arising from the satellite images is due to the presence of clouds. Clearly, since in general the MCC techniques detect surface (or near-surface) currents associated to well define patterns, the presence of clouds alters this capability.

Another important problem in real images is represented by the noise that influences the detectability of current vectors in the scene. In this work different denoising techniques, similar to those adopted by other authors (Kamachi, 1989; Marcello *et al*, 2008), have been tested in order to reduce the effect of noise. In particular, three filters have been applied to satellite sequences: mean, Gaussian and median. However, while on the one hand the use of a filter reduces the noise in the image, on the other hand it may produce smoothing effects that blur the patterns tracked by MW-MCC. In order to improve the pattern detectability, a sharpening filter has been also applied and tested.

A third source of errors in the dataset of MODIS images is caused by the effect called striping or banding. It appears as a repetition of linear stripes in the images, and can make it very difficult to process the satellite sequences. Although it is possible to reduce striping by the application of some enhanced algorithms (Weinreb *et al*, 1989; Antonelli *et al*, 2004; Rakwatin *et al*, 2007; di Bisceglie Episcopo *et al*, 2009; Bouali, 2010; Mikelsons *et al*, 2014), it is generally not possible to completely eliminate this effect, and the images must sometimes be discarded.

A last problem in satellite images is georeferencing. Its effect is considered negligible for the MODIS imagery, so no geometric correction or co-registration procedure is implemented.

As a consequence of the above limitations, the number of useful MODIS images is greatly reduced. The time period chosen for analysis was during the summer, because of the relatively clear sky conditions. In this period, 47 pairs of images (about 15 per month) were considered suitable for the MW-MCC application (about 26% of the total).

After the selection of a sequence of images and their filtering, it is fundamental to apply a calibration procedure, as already discussed for synthetic imagery. This process is very important in order to determine the correlation threshold for the false alarm probability, and the correct significance level.

In the application of MW-MCC to MODIS imagery, it is also very important to note that multiple spectral bands are available for every image, which are obtained from reflection (daytime only) and emission data. It is therefore possible to apply the MW-MCC algorithm to the same scene several times, as many as the number of spectral bands, in this way increasing the number of current vectors found. The distinct spectral bands reflect the behaviour of different physical/chemical phenomena, but not all of them can be considered valid tracers for the ocean currents (Shao *et al*, 2011). One of the aims of this work is to determine whether or not a spectral band can be used by the MW-MCC algorithm as a good tracer for the ocean circulation. A systematic application of a MCC algorithm to several spectral bands (multi-channel analysis) is done for the first time.

The area covered by the research includes the Tyrrhenian Sea, Ligurian Sea, and part of the Balearic Sea

up to the Gulf of Lion. Due to the lack of systematic current measurements in this area, an extensive error analysis of the MW-MCC results has not been performed. However, some data from the HF radar system near Toulon have been used for the validation of the MW-MCC results in a case study. Since further suitable observation data were not available, some comparisons between the MW-MCC results and numerical hydrodynamic model simulations have been also done.

In general, the coherence of the resulting circulation flow, the high number of current vectors found, the agreement among different spectral bands, the conformity with the currents measured by HF radars or simulated by hydrodynamic models, show the validity of the technique.

Another HF radar system has been just installed by the Regione Toscana in Tuscany, and will soon be operational. Therefore, in the near future, these new data will allow a more systematic validation of the MW-MCC results in the Tuscan Archipelago.

The paper is organized as follows. Section 2 reports the datasets used. Section 3, after a brief review of the MW-MCC method, describes the pre-processing, processing, and post-processing phases of the algorithm. In the pre-processing phase an image destriping and filtering are performed. Note that a filtering was not implemented in the previous work on synthetic images (Doronzo *et al*, 2015), due to their noise-free nature. Instead, the processing and post-processing steps are the same as those applied to synthetic images, so are not discussed in detail. The calibration phase is illustrated in Section 4. A broad discussion of the MW-MCC results is reported in Section 5. First, an analysis is done of the current data obtained by multi-channel approach; the differences between results obtained using either daytime or night time sequences are then studied. Finally, some examples of the current flows obtained by MW-MCC, and the case study of a comparison between HF radar measurements and MW-MCC data are discussed. Section 6 provides the conclusions.

## 2. Data

### 2.1 Satellite Dataset

The multi-band images used in this work were produced by the Moderate Resolution Imaging Spectroradiometer (MODIS), which is on board the Aqua and Terra satellites launched by NASA. More specifically, the subset considered is the MODIS L1B, which has calibrated radiances at 1.1 km (NASA MOD021). Images in both reflected and emissive solar bands have been used; more precisely, the phytoplankton and biogeochemical bands (band numbers: 8–16 at 405–877 nm), and some ST/SST bands (band numbers: 20–23 at 3660–4080 nm, and 29–32 at 8400–12270 nm).

Other products, for example NOAA images, have not been used at the moment, since they require a more extended pre-processing analysis due to known navigation problems (Alexanin *et al* 2005) that are not easily solvable and make them not appropriate for a direct MW-MCC application.

### 2.2 HF Radar Dataset

This paper reports a case study of a comparison between data from an HF radar system near Toulon, and the MW-MCC results. The HF radar system was installed within the framework of the MOOSE project (Institut Méditerranéen d'Océanologie). The sites of the radars are in Fort Peyras (E/R) du Sémaphore du cap Bénat (R) and Sur L'Ile de Porquerolles (E). The surface currents are produced by combining radial information from each site, and cover an area of up to 96-113 km from the coastline. The resolution of the current velocity vectors is 3 km, but their accuracy depends on distance from the coast. Maps of currents are provided every 20 minutes. The archive is available starting from December 2011 (retrieved from http://hfradar.univ-tln.fr).

### 2.3 Model Dataset

In this paper comparisons between numerical ocean model simulations and MW-MCC results are performed. The data exploited come from two different hydrodynamic models.

The first one is the Mediterranean Forecasting System (MFS), physical reanalysis component, of the Copernicus Marine Environment Monitoring Service (CMEMS) (http://marine.copernicus.eu/). The MFS model is supplied by the Nucleus for European Modelling of the Ocean (NEMO), with a variational data assimilation scheme (OceanVAR) for temperature and salinity vertical profiles and satellite Sea Level Anomaly along track data. The model horizontal grid resolution is 1/16° (ca. 6–7 km), and the unevenly spaced vertical levels are 72. The current reanalysis data are released as monthly and daily means.

In order to make a comparison with hourly data, the short-term simulations of a sub-regional implementation of the Regional Ocean Modeling System (ROMS), an incompressible, free surface, hydrostatic, primitive

equation circulation model (Shchepetkin and McWilliams, 2005), have been also used. This model is configured within the area defined by the coordinates 7.20°–16.25° E, and 36.67°–44.45° N, with a horizontal resolution of 2 km and a vertical discretization of 30 s-levels. The topography used for the bathymetry is based on the EMODNET dataset, with a resolution of about 500 m. Air-sea interactions are imposed using fluxes derived from an implementation of the WRF-ARW model over the central Mediterranean area at 3 km resolution, implemented at LaMMA and using ECMWF analysis data as initial and boundary conditions. Boundary and initial conditions for the hydrodynamic model are taken from the assimilated MFS model data available at the CMEMS.

## 3. The Multi-window MCC Algorithm

The classical MCC method applied to ocean circulation is a procedure for reconstructing the surface velocity field. The technique estimates the displacement of small regions of passive tracer patterns between two sequential images by computing the maximum cross-correlation (MCC) among small rectangular windows (template windows) in the first image and those in the second one.

The basic MCC technique is explained in detail in the literature (Emery, 1986; Garcia and Robinson, 1989; Wahl and Simpson, 1990). It was originally used on sequential thermal images, but, more recently, some authors have also applied MCC to other spectral bands (Prasad, 2002; Crocker, 2007; Marcelo, 2008).

In this paper, MCC is tested on the Mediterranean sea, and, more specifically, in the area of the Tyrrhenian Sea, Ligurian Sea, and part of Balearic Sea up to the Gulf of Lion. Here, the presence of many islands in the Tuscan Archipelago makes application of the MCC difficult in its classical form. An attempt has therefore been made to develop an improved and more robust algorithm. This algorithm, called MW-MCC, has already been described and tested on synthetic imagery in a previous paper (Doronzo *et al.*, 2015). Basically, the MW-MCC algorithm differs from the classical MCC approach because it uses multiple template windows with different sizes.

The MW-MCC consists of three phases: pre-processing, processing and post-processing. While the pre-processing phase is very similar to the preliminary treatment of satellite images before the application of any MCC algorithm, the processing and post-processing phases contain the main differences between the MW-MCC and the classical implementation. However, since the processing and post-processing phases are the same as those already extensively discussed in Doronzo *et al.* (2015), only a brief review of their main features will be given here.

### 3.1 Pre-processing

In the pre-processing phase, both destriping procedures and image filtering techniques are adopted. The literature concerning destriping is quite extensive, but in this paper the focus will be only on a particular algorithm (Gumley, 2005). Instead, in the subsection about image filtering, a comparison among three common denoising filters will be made, and their effects on satellite sequences will be shown. Filter efficiency will then be evaluated on the basis of the number of velocity vectors found by MW-MCC.

#### 3.1.1 Destriping

Striping, also known as mirror banding, is a common problem in MODIS images. It appears as regular stripes on the picture, which alter the quality of images and cause difficulties in the application of MW-MCC. It is a consequence of an independent calibration of the different detectors at 1000 m resolution inside the MODIS sensor. The problem is more evident in the presence of bright targets, with reflectance values high enough to bring the sensor close to its saturation mode. A typical case of striping can be seen in oceanographic images affected by sun glint or strong atmospheric effects. Many authors (Simpson and Yhann, 1994; Algazi and Ford, 1981) have demonstrated that other factors like source spectral distribution and polarization, or random noise in the internal calibration system can also play a role. For these reasons stripes are in many cases not uniformly distributed in the image, and may affect only specific areas or spectral bands.

Many destriping algorithms have been proposed in the literature, and can be classified in two different classes.

Some authors (Crippen, 1989; Srinivasan *et al*, 1988; Pan and Chang, 1992; Simpson *et al*, 1995; Simpson *et al*, 1998; Chen *et al*, 2003) tested a digital filtering on different satellite and sensor sequences, assuming periodicity of stripes, and removing them with a frequency analysis. This approach is very simple, but introduces blurring effects in imagery, and a loss of radiometric accuracy.

Other authors (Horn and Woodham, 1979; Weinreb

*et al*, 1989; Gumley, 2002) took advantage of the statistical properties of each detector. They use histogram matching techniques by assuming that the distribution of the intensity of the earth's radiation incident on each detector will be similar. Therefore a reference empirical distribution function (EDF) is chosen, corresponding to one of the most stable and best quality detectors, and the other EDFs are modified to be the same as the reference one by generating appropriate normalization tables. The output of each detector is then adjusted by using these normalization tables. These statistics based methods are more common, and give good results, although there is a limit to their performance due to the strong assumptions on which they rely.

The destriping technique adopted in this work lies in the second class, i.e., it is based on matching EDPs. The software IMAPP provided by the Wisconsin-Madison University (Huang *et al*, 2004), distributed under open license, has been used.

The result of the application of the IMAPP routines is reported in Figure 1.

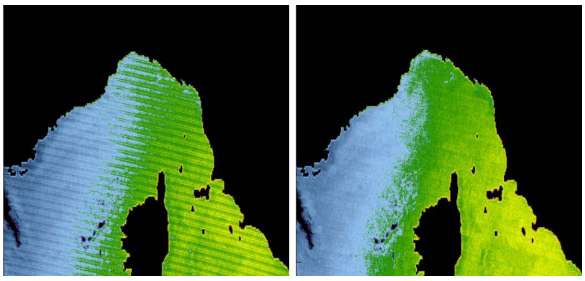

**Figure 1.** Striped image (Left) and destriped image with IMAPP routines (Right). The picture represents an arbitrary image of the emissive band 24.

Although in this case destriping is very effective, the procedure sometimes leaves residual stripes. The result can also depend on the spectral band chosen. Therefore after the destriping process, a further selection of the images must be made.

### 3.1.2 Image Filtering

The presence of noise in satellite imagery makes it difficult to detect the current velocities correctly. In fact, application of the MW-MCC algorithm to images with distorted or ill-defined patterns, without a preliminary denoising phase, produces many spurious vectors. As a consequence a preparatory image filtering is very important, and an accurate choice of filters must be made. In order to choose the correct filter, it is firstly necessary to identify which kind of noise is affecting the images.

Filters can be defined by a typically rectangular matrix, 3×3 or larger, also called a mask. The filtering process in the spatial domain associates the mask coefficients to a subset of pixels adjacent to the filtered one, and, in the case of a linear spatial filter, the new value for the filtered pixel is given by a sum of products of the mask coefficients and the corresponding image pixel values in the area spanned by the mask. In this paper, the effects of different mask sizes, in particular 3×3 and 5×5, will be considered. The mask form can also be changed (e.g., circle or rectangle), but the effect of this will be not discussed.

The choice of filters was based on the assumption that, according to the literature, the noise in MODIS satellite images is typically of two types: salt-and-pepper, and Gaussian. In the following, three spatial filters, appropriate for these kinds of noise, will be discussed (Carvalho, 2012).

The first one is a Standard Median Filter (SMF), which typically provides good noise-reduction capabilities in the presence of impulse noise like salt-and-pepper (Gonzales and Woods, 2002). The second one is a Mean Filter (MF), which is the simplest kind of filter, and is suitable for smoothing purposes. It consists of a simple arithmetic average of all masked pixels. This operation reduces the noise in the image and at the same time smooths the edges exploited by the MW-MCC algorithm during pattern tracking. The third one is a Gaussian Filter (GF). In this case, although some smoothing effects are still present, the application of the mask yields a weighted average that better preserves the pattern contours. It is also possible to increase or decrease the smoothing effect by increasing or decreasing the Gaussian standard deviation. In the literature (Al-amri, 2010) it is usually assumed that the MF and GF filtering procedures give the best results when applied to satellite images affected by Gaussian noise.

Finally, once the noise has been removed, a 'sharpening' derivative filter can be applied, in order to enhance the pattern edges. Here a 3×3 sharpening filter has been used, defined by the matrix:

$$\frac{1}{(a+1)}\begin{bmatrix} -a & a-1 & -a \\ a-1 & a+5 & a-1 \\ -a & a-1 & -a \end{bmatrix}$$

where the value of $\alpha$ has been taken as equal to 0.2.

In the following, the above filters will be tested in order to identify the best choice for our purposes. Even if the difference among the resulting images after denoising is barely visible to the naked eye, the preliminary application of these filters to satellite sequences may give very different final results. If the denoising process is followed by the application of the sharpening filter, once again the difference is barely visible. So, in order to evaluate the final effects of this filtering procedure, a statistically significant amount of images must be processed, and the number of vectors obtained after the MW-MCC computations observed. This number is an index of the capability of the algorithm to identify the edges of the filtered pattern. Therefore, the larger is the number, the better is the filter.

The number of vectors found by applying the MW-MCC algorithm, with different combination of filters (mask size 3×3), to about 40 different pairs of images in the spectral band 23, is reported in Figure 2. Similar results can be found for other spectral channels, and/or a different mask size (5×5). An improvement due to denoising is evident for all three kinds of filters, although the combination between denoising (e.g., Gaussian) and sharpening gives results similar to the case without any filtering. This probably depends on a well-known problem in the application of sharpening filters, i.e., sharpening enhances the residual noise that has not been removed by the denoising filter, and this can give rise to a loss in image quality (Gonzales and Woods, 2002).

A summary of the above analysis is reported in Table 1, which gives the mean values of the number of vectors obtained.

The Table 1 shows that the MF filter is probably the best one according to the criterion adopted. The

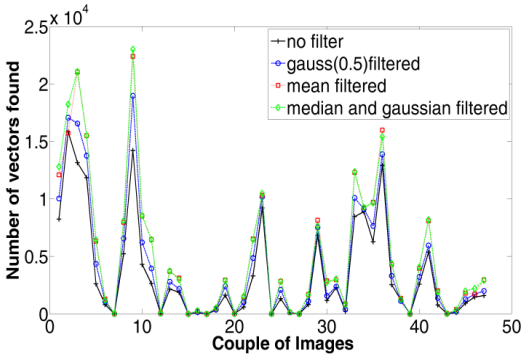


**Figure 2.** Number of current vectors obtained after the application of the MW-MCC algorithm, with different combinations of filters (mask size 3×3), to various pairs of images in the spectral band 23.

**Table 1.** Number of current vectors for different filtering[1]

| Band 23 | Gauss | Mean | Median | Gauss +Sharpening | Median + Gauss | No filter |
|---|---|---|---|---|---|---|
| 3 pxls | 4228 | 5098 | 4817 | 3751 | 5176 | 3457 |
| 5 pxls | 4229 | 5760 | 5552 | 4786 | 5768 | 3457 |

[1]Mean values of the number of current vectors obtained after application of the MW-MCC algorithm, with different combinations of filters, to about 40 different pairs of images in the spectral band 23 for different mask size (3 and 5 pixels). The GF standard deviation is 0.5.

GF filter behaves like the MF, if the Gaussian standard deviation is high enough, while if the standard deviation decreases, the filter becomes too selective, and its performance decreases. The SMF filter works fine in the presence of impulse noise, but it has slightly lower performances with Gaussian noise, unless it is applied in combination with MF or GF.

It is also possible to show, for each vector found in Table 1, the corresponding MCC values. Figure 3 represents, as an example, a sub-image of MCC matrix relating to vectors found by images non-filtered and with MF applied, respectively. The latter values are some percentage points higher:

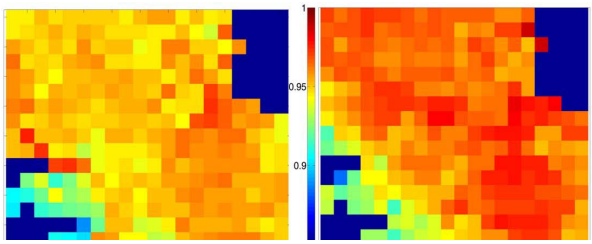


**Figure 3**. Example of maximum cross-correlation values obtained by non-filtered (left) and mean filtered (right) satellite sequences. Since MW-MCC is based on multiple template windows with different sizes, this plot represents a mean of multiple MCC matrices.

The higher MCC values in Figure 3 demonstrate that the vectors found after filtering arise from more robust template matching. It should be noted that the resulting MCC values matrix, shown in Figure 3 is obtained by averaging multiple MCC matrices, each of which is calculated by using different size template windows (16, 18, 20, 22, 24 pixel size) on the whole sequence.

The results obtained with a 5×5 mask size are also reported. This improves vector detection, probably due to an increase of smoothing effects and noise reduction. The problem is that image resolution is also altered, and this alteration grows quickly by increasing the mask size. It follows that by using larger mask

sizes, the resolution and accuracy of the computed current vectors can get worse.

Another negative effect of a larger mask is the increasing of NaN values along the coastline, because a larger number of land pixels enter the filtering area. As a consequence, the mask size should be very carefully modified.

In conclusion, since Table 1 shows that the advantage of using a combination of filters or larger masks is not very significant with respect to the results of MF with a 3×3 mask, which is simpler and less time-consuming, only this filter will be used in the following analysis.

### 3.2 Processing

The processing phase is in two steps.

The first one, as in any MCC algorithm, is a scanning of a search window based on a FFT method, for the calculation of normalized cross-correlation coefficients.

In the second step, the main differences between MW-MCC and a traditional MCC approach come into play. In particular, the use of multiple template windows: in this algorithm, after the first scanning, the size of the template is increased, and a further scanning operation is performed. Here the scanning is not complete, in the sense that the new larger template window will be moved only on positions where a velocity vector has been found in the first step. This operation is then repeated with larger and larger templates until a given number of windows has been reached. All scanning operations give candidate velocity vectors that must be validated in the post-processing phase. The smallest of these windows is referred as 'reference window', and its size as the template window amplitude. The choice of the sizes and number of these windows is based on many tests done for real images, and is a compromise between algorithm robustness and required resolution. In the following, we use a 16 pixels template window amplitude, and five windows of increasing size, up to 24 pixels.

### 3.3 Post-processing

The processing phase of MW-MCC gives a number of vectors equal to the number of different template windows, i.e., five in this case, for each position where it finds results. The post-processing is instead a validation phase, where the calculation is made of a single valid final velocity vector for each position. First of all, each group of vectors in each position is tested, and it is accepted only if some conditions are satisfied (Doronzo *et al*, 2015). The final velocity vectors are then obtained by averaging all vectors within each group.

## 4. Calibration

It has been shown in Doronzo *et al.* (2015), which the calibration is a critical step, because it can identify an important threshold, i.e., a cut-off value for the maximum cross correlation that allows false positive matching to be discarded.

The approach followed is based on a numerical statistical analysis of the images. The threshold can be obtained from the histogram of the maximum cross correlations calculated among all possible templates in the scanning area of a first image and those in areas spatially and temporally uncorrelated (null hypothesis) in a second image, and this is done over many different images. This threshold represents a noise level, and above this level the correlation can be considered significant.

It should be noted that the cut-off value depends on many factors, like quality of images, satellite sensor, spectral band and template size, plus image brightness that differs for seasonal, daytime or night time sequences. Thus, in order to obtain significant results, it is important to make a new calibration every time one of these parameters changes.

Two calibration histograms are shown in Figure 4: the first for 6 pixel template window amplitude, the second for 26 pixel template window amplitude. Since the analysis on MODIS images has shown very similar results for the histograms of different spectral bands, only spectral-band-averaged histograms are used to calculate the thresholds.

The integral of the histogram to the right of the threshold (red line), divided by the total number of maximum cross correlation values found, is called false alarm probability, which is complementary to the level of significance.

Figure 4 shows that the false alarm probability depends on the template size: in order to maintain the same level of significance, the threshold must be increased with smaller template sizes. For the 6 and 26 pixel templates the same threshold (0.9) corresponds to a false alarm probability of about 40% and 1.2% respectively; these percentages also take into account the maximum cross correlation values removed by the MW-MCC algorithm in the post-processing phase, which are not represented in the histogram. This is due

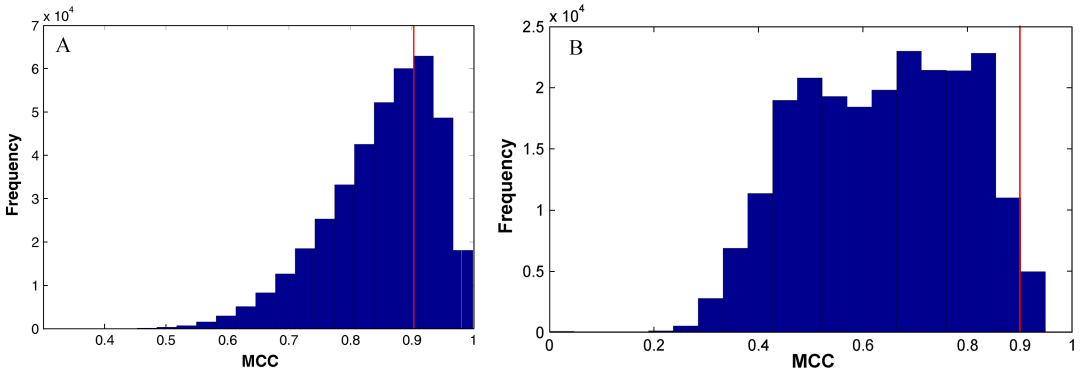


**Figure 4.** Spectral-band-averaged histograms of maximum cross correlation values with the cut-off threshold (red line): (A) for 6 pixel template window amplitude, (B) for 26 pixel template window amplitude.

to the fact that, since small templates contain simpler structures, a possible correlation is more likely. As a consequence, very small templates should not be used in classical MCC algorithms, and for the present-day satellite images, 20–26 pixel template window amplitudes are the most appropriate. Due to the peculiarity of the MW-MCC algorithm, reference windows smaller than that instead can be used.

In this work, multiple template sizes between 16 and 24 pixels have been adopted, and a false alarm probability equal to 1.5%, with the corresponding threshold between 0.8–0.9.

## 5. Results

In this work, 47 pa irs of MODIS images for each spectral band (31 bands), i.e., a total of about 1500 pairs, have been processed. The images were recorded during the summer in quite clear sky conditions, and represent about 26% of all MODIS scans over the area of interest, which includes the Tyrrhenian Sea, Ligurian Sea, and part of the Balearic Sea. As already mentioned, distinct spectral bands reflect the behaviour of different physical/chemical phenomena, and it is possible to apply the MW-MCC algorithm to the same scene as many times as the number of spectral bands. For the first time, the results of a systematic application of the MW-MCC algorithm to several spectral bands (multi-channel analysis) are reported, in order to determine whether or not a spectral band can be used by the MW-MCC algorithm as a good tracer for the ocean circulation. The differences between daytime and night time results are then discussed. Lastly, some examples are shown of the current flows obtained by MW-MCC, and the case study of a comparison between HF radar measurements and MW-MCC data is analyzed.

### 5.1 Multi-channel Analysis

If the number of vectors obtained by MW-MCC is an index of the capability of the algorithm to identify the edges of patterns, an indication about the adequacy of the various spectral bands to be used as tracers for the surface circulation can be obtained by plotting this number versus the band number.

Daytime reflected solar bands (band numbers: 8–19, and 26 at 405–1390 nm), used for example for the detection of phytoplankton and other biogeochemical tracers that can be found in a layer of a few meters below the sea surface, give rise to poor pattern gradients and many corresponding maximum cross correlation values appear lower than the cut-off threshold. Furthermore many of these parameters, such as chlorophyll, usually have much higher concentrations near shore, and in order to obtain more visible patterns in deeper waters, a preparatory non-linear scaling, which was not done here, should probably be applied to MODIS images before the MW-MCC processing. This behaviour is confirmed by the results reported in Figure 5, where the columns of

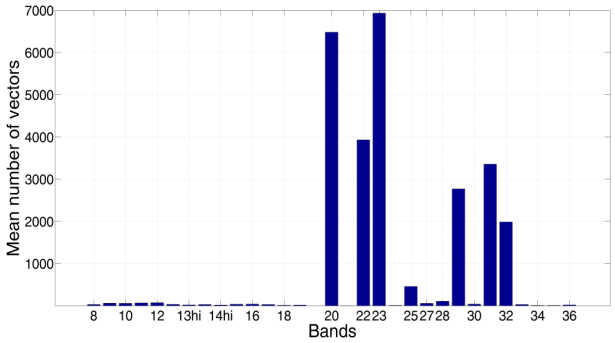


**Figure 5**. Mean number of vectors obtained by MW-MCC from images corresponding to different spectral bands versus band number.

the bar chart corresponding to these bands are very low. Instead, some emissive bands produce quite evident pattern gradients, in particular the mid- infrared bands 20, 22 and 23. This behaviour, besides possible physical-biochemical considerations, suggests that thermal features can be better tracers than biogeochemical properties. Moreover, the application of MW-MCC to ocean color images is not only less efficient for the reason above, but also because a lower number of images is available with respect to infrared images, since they are produced only during daytime.

It should be also noted that bands 22–23 are typically used for the calculation of short-wave SST, e.g., the MODIS ocean colour products distributed by the Ocean Biology Processing Group (OBPG) at NASA's Goddard Space Flight Center. For these reason in the past many authors applied MCC techniques primarily on SST products.

In Figure 5 it is also shown that the thermal infrared channels 29, 31, 32, give good results, in accordance with other authors (e.g., Bowen *et al*, 2002; Crocker *et al*, 2007), while other emissive bands, like the ones in the interval 24–28 (4433–7475 nm) and above 32 (13185–14085 nm), produce very few vectors, probably due to weak pattern gradients, at least in the sea area studied. Instead, the poor results of bands 21 (3929–3989 nm), 30 (9580–9880 nm), and 36 (14085–14385 nm) are due to the fact that the corresponding images are affected, more than others, by random noise and striping.

As a consequence, if the bands 21 and 30 are used in combination with other thermal bands in order to produce SST products (e.g., Esaias *et al*, 1998; Justice *et al*, 2002; Minnett and Barton, 2009), the application of MCC techniques to them could give some problems.

Figure 5 clearly shows that most of the current vectors found come from images relative to the spectral bands 20, 22, 23, 29, 31, and 32, which seem the most appropriate for MW-MCC. In particular, the analysis reported in the next sections has been made by using the three bands that give best results, i.e., 20, 22, 23.

### 5.2 Daytime and Night Time Sequences

In Doronzo *et al.*(2015), it was shown that factors related to thermal exchanges in the water column can affect the MW-MCC results, as was evident by a comparison between night time and daytime, or winter and summer data. In this section, the results obtained by night time and daytime image sequences are further discussed.

Figure 6 and Figure 7 report the number of vectors obtained by MW-MCC for each spectral band versus band number for daytime and night time, respectively. Increments of about 65% for the vectors in band 20, and about 30% for those in bands 22–23 are observed during the night. Although no systematic validation of the computed currents has been done, the strong coherence among the vectors, in significant agreement with some well-known current flows, indicate that the MW-MCC method works better when applied to MODIS night time images.

Thermal surface instability is probably not the only reason for these remarkable differences. It could also be due to the fact that some spectral bands, in particular those near 4000 nm, are affected by bright reflective sources, such as sun glint, during daylight hours. This is a known issue in remote sensing of water surfaces, and has been investigated by many authors (e.g., Rainey and Hallenborg 2013). Some techniques have also been suggested to reduce this effect (e.g., Kay *et al*, 2009), but they have not been applied here.

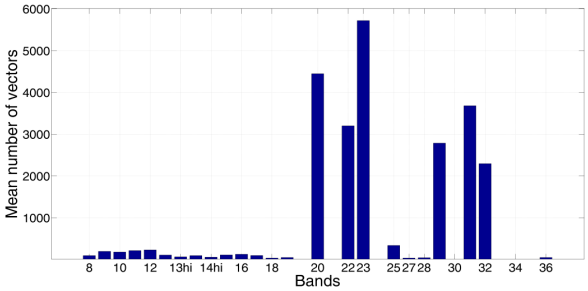


**Figure 6**. Mean number of vectors obtained by MW-MCC for each spectral band versus band number, in daytime.

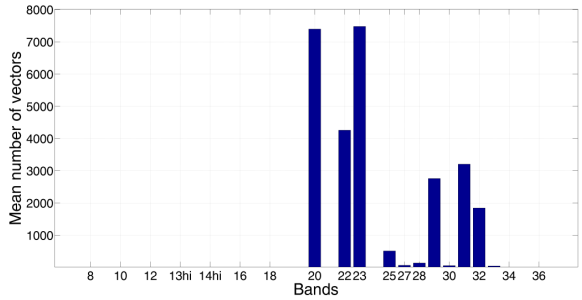


**Figure 7**. Mean number of vectors obtained by MW-MCC for each spectral band versus band number, at night.

### 5.3 MW-MCC Applications

Figure 8 reports two examples of application of MW-MCC to satellite images derived from three different spectral channels, in the area of the Tyrrhenian, Lig-

urian, and Balearic Seas. The vectors have been downsampled for a better visualization.

The middle and bottom pictures are zooms of the top ones, as shown in the insets. Figure 8 clearly shows that the multi-band approach gives some advantages. For example, it allows current vectors to be calculated even when some pattern displacements are not detectable in certain spectral bands, but can be observed in others. It is also useful as a validation tool, if the assumption is made that there must be coherence among vectors obtained by different spectral bands. In fact, the vectors plotted show a good spatial coherence, and they sustain the validity of the MW-MCC results in real applications.

It should also be noted that the currents reported in the middle and bottom zoom pictures are consistent with the main flows known in those areas. Let us consider, for example, the Liguro-Provençal basin, located

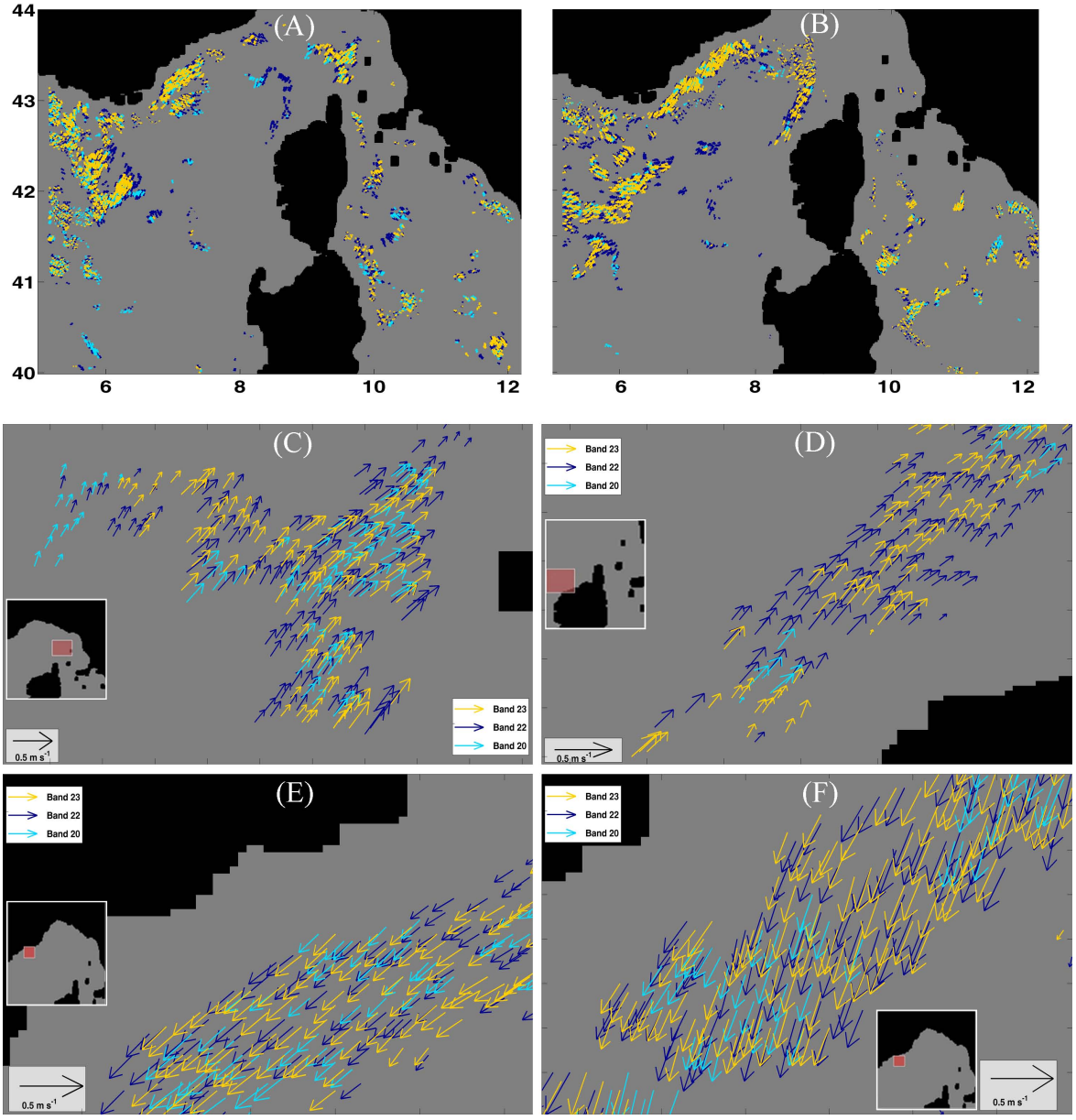


**Figure 8.** Examples of vectors obtained by applying MW-MCC to two pairs of MODIS scenes: (A) 2 Sept 2014 21.50 UTC, and 3 Sept 2014 02.05 UTC; (B) 3 Sept 2014 20.55 UTC, and 4 Sept 2014 01.10 UTC; (C) zoom of Figure 8A to the North-East of Corsica; (D) zoom of Figure 8B to the North-West of Corsica; (E) zoom of Figure 8(A) in the Gulf of Lion; (F) zoom of Figure 8B in the Gulf of Lion. The different colours result from the application of MW-MCC to different spectral bands: 20 (light blue), 22 (dark blue), and 23 (yellow).

in the north-western Mediterranean Sea off the coasts of Italy and France, and connected to the south-east with the Tyrrhenian Sea through the Corsica Channel. The main circulation in the basin is well known (e.g., Istituto Idrografico della Marina, 1982; Millot, 1999; Schroeder *et al*, 2011), and consists of a basin-wide cyclonic gyre. In the Corsica Channel, the northward Eastern Corsican Current (ECC) brings Tyrrhenian water into the Ligurian Sea, while, west of Corsica, there is another northward current, the so-called Western Corsican Current (WCC), which is part of the large cyclonic circulation. The confluence of the ECC and the WCC north of Corsica forms the Northern Current, which flows west along the Italian, French and Spanish coasts. This behaviour is in agreement with the results in Figure 8.

The top pictures in Figure 8 also show that there are often areas with missing vectors. This is probably due to a poor brightness gradient or to some striping. Furthermore, some areas, like Tuscan Archipelago, are less suitable for the application of MW-MCC because the presence of many islands reduces the open sea surface and the land pixels contaminate search and template windows, giving many null values. Moreover, coastal water phenomena, such as upwelling, could give rise to pattern deformations not related to horizontal current flows. As a consequence, better results can be found in larger open areas, like the Balearic Sea and Southern Tyrrhenian Sea.

### 5.4 MW-MCC Comparison with HF Radars and Numerical Ocean Circulation Models

In order to validate current flows calculated by MW-MCC a comparison has been made with HF radar data. However, due to a lack of observations in the area and period studied, a spatial and temporal overlap of the MW-MCC and HF radar data was possible in only one case. In particular, a map from the HF radar system near Toulon, installed within the framework of MOOSE project, as described in Section 2, has been used. Moreover, since the MOOSE radars only provide data quite close to the shore, just a small spatial overlapping was feasible. In the end, the MW-MCC current map obtained by the pair of MODIS images corresponding to 27$^{th}$ Jul 2014 at 10.25 UTC, and 27$^{th}$ Jul 2014 at 12.10 UTC, was compared with the HF radar map of 27$^{th}$ Jul 2014 at 11.01 UTC, taken from the Mediterranean Institute of Oceanography (MIO) website (http://hfradar.univ-tln.fr). This comparison is reported in Figure 9.

The general agreement in intensity and direction between the two maps is quite good. On both maps, the currents at the centre of the area reach speeds of about 0.65 m/s, while a decrease in current intensity is observed at lower and higher latitudes. Furthermore, the flows are both mainly directed towards

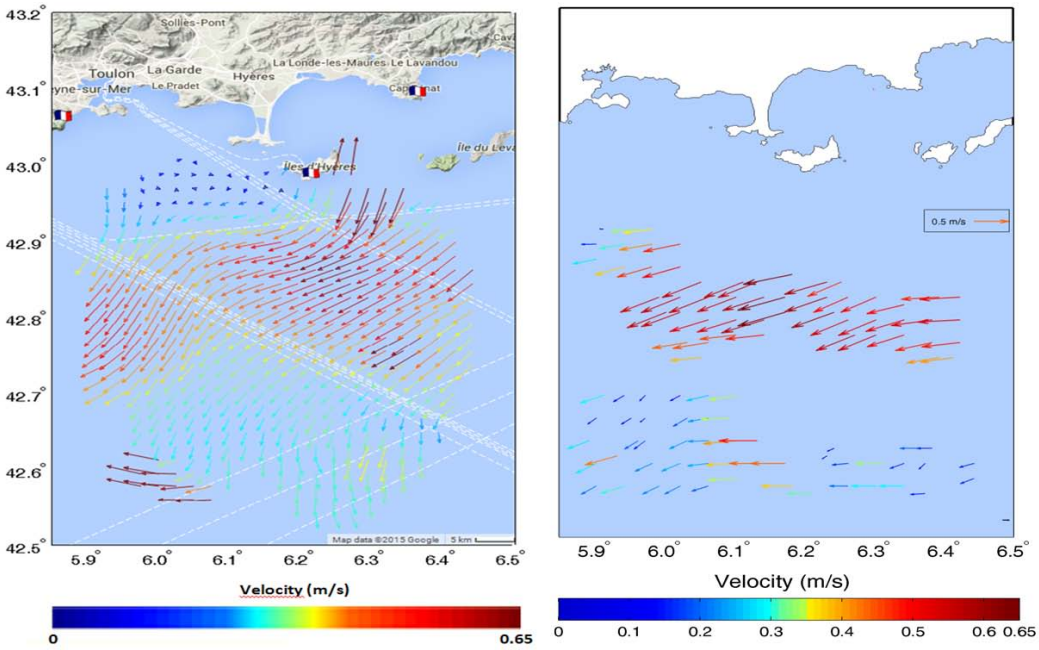


**Figure 9**. (Left) MOOSE HF radar map of 27$^{th}$ Jul 2014 at 11.01 UTC, taken from the MIO website; (Right) MW-MCC current map obtained by the pair of MODIS images corresponding to 27$^{th}$ Jul 2014 at 10.25 UTC, and 27$^{th}$ Jul 2014 at 12.10 UTC.

south-west, although there are some degrees of difference between them. However, it should be noted that these differences are similar to those observed in the systematic analysis made by synthetic images in a previous paper (Doronzo *et al*, 2015). Moreover, it must be considered that while the radar data represents an hourly average of a nearly continuous measurement, MW-MCC results are calculated only by two instantaneous satellite images that were taken almost two hours apart. Therefore, in this case study, neither the time interval nor its length coincide exactly. A more systematic validation of the MW- MCC results, based on an HF radar system just installed in Tuscany, will be performed in the near future.

Since further suitable observation data were not available, in order to increase the confidence in the MW-MCC results, some comparisons with numerical ocean circulation model simulations have been performed in two different areas: the first one in the Tyrrhenian Sea, and the second one in the Ligurian Sea, north of Corsica.

The first comparison has been made between the results of MW-MCC and the reanalysis from the MFS model of CMEMS for the 28$^{th}$ Sep 2014 at 00:00 UTC. Unfortunately, for September 2014 only daily data are available from CMEMS. Therefore, a valid comparison with MW-MCC is possible only if a preliminary time average of the MW-MCC currents is done. More precisely, four pairs of images between 26$^{th}$ Sep 2014 at 21.05 UTC, and 28$^{th}$ Sep 2014 at 01.55 UTC have been used. The MW-MCC current image has been calculated by the time average of the four series of current vectors obtained by the four pairs. Before the time average process, a spatial mean with 6-pixel windows has been also performed. Finally, for a better comparison, the model vectors have been interpolated on the same grid of MW-MCC vectors. The results are reported in Figure 10A and B. The estimated mean absolute errors are 19 cm/s (about 56%) in magnitude, and 12° in direction. The agreement in direction is very good, but the error in magnitude is quite high.

A second comparison has been still made with the MFS model data, but for the 3$^{rd}$ Sep 2014 at 00:00 UTC. In this case, four pairs between 2$^{nd}$ Sep 2014 at 21.50 UTC, and 4$^{th}$ Sep 2014 at 01.10 UTC have been exploited. Here the estimated mean absolute errors are 13 cm/s (about 47%) in magnitude, and 38° in direction. In this case the error in magnitude is a little better, but the mean direction is worse than before.

In conclusion, although there is an overall reasonable agreement, the differences are not negligible. This can depend on at least two main factors: firstly, the numerical ocean models, although assimilated, are affected by intrinsic errors; secondly, similarly to the case of radar data, while the model output represents a temporal daily average of a continuous simulation, MW-MCC results are calculated only on a few instantaneous satellite images, since pairs of images covering all hours of the day are not available.

In order to verify this latter hypothesis, a short term higher resolution simulation with a numerical regional ocean model (ROMS) nested on the MFS-CMEMS data has been performed. Then, the ROMS results for the 3$^{th}$ Sep 2014 at 00:00 UTC have been compared with the MW-MCC currents obtained by a single pair of satellite images taken the 2$^{nd}$ Sep at 21:50 UTC, and the 3$^{rd}$ Sep at 02:05 UTC. In this case the estimated mean absolute errors are 7 cm/s (about 19%) in magnitude, and 14° in direction, in agreement with the hypothesis above.

## 6. Conclusions

This paper reports the results of a systematic application of the Multi-Window MCC algorithm to a large number of MODIS multi-band products. In particular, 31 spectral bands have been considered, and 47 pairs of images for each band have been processed. The area concerned includes the Tyrrhenian Sea, Ligurian Sea and part of the Balearic Sea. The main advantages of using a multi-band approach are: the capability to calculate current vectors even when some pattern displacements are not detectable in certain spectral bands, but can be observed in others; the possibility to use it as a validation tool, assuming that there must be coherence among vectors obtained by different spectral bands.

Indeed, the results of this study have shown that there is a good coherence among most of the vectors obtained by different spectral bands, although there are also a few incoherent ones. If this coherence requirement were to be used as a constraint and implemented in the algorithm, it would probably further increase the reliability of the MW-MCC algorithm. Work on this is in progress.

A purpose of this analysis was also to determine whether or not a spectral band can be considered a good tracer for the ocean circulation. The result obtained in the studied sea area is that images relative to the MODIS mid-infrared bands 20, 22 and 23 are the

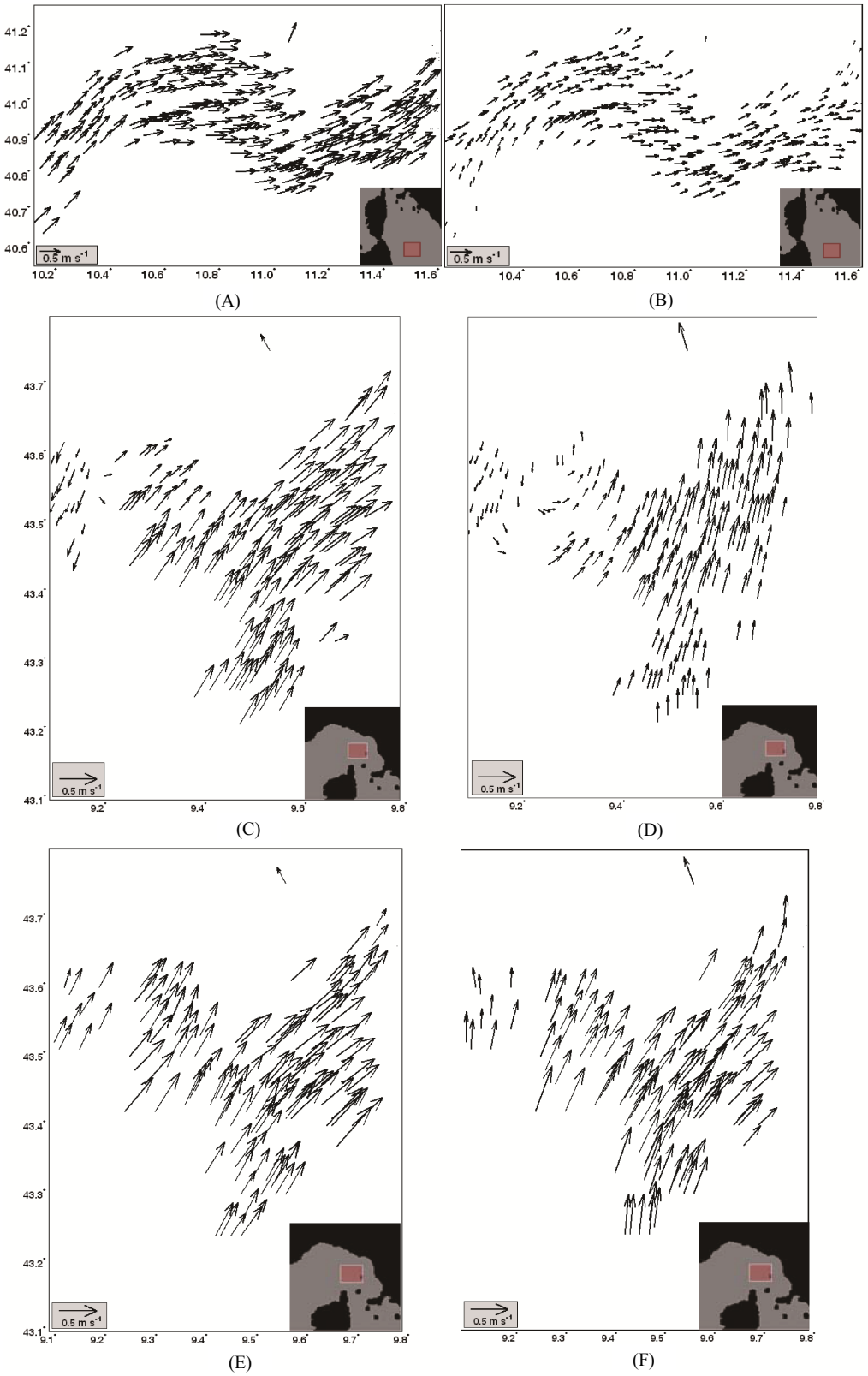


**Figure 10.** (A) MW-MCC mean currents between 26th Sep 2014 at 21.05 UTC, and 28th Sep 2014 at 01.55 UTC; (B) MFS daily mean currents for 28th Sep 2014 at 00:00 UTC; (C) MW-MCC mean currents between 2nd Sep 2014 at 21.50 UTC, and 4th Sep 2014 at 01.10 UTC; (D) MFS daily mean currents for 3rd Sep 2014; (E) MW-MCC current map obtained by the pair of MODIS images corresponding to 2nd Sep at 21:50 UTC, and 3rd Sep at 02:05 UTC; (F) ROMS current map for 03th Sep 2014 at 00:00 UTC.

most appropriate for MW-MCC. Bands 22 and 23 are typically used for the calculation of short-wave SST. Other SST products, based on thermal bands 21 and 30 appear less suitable for MCC methods. The thermal bands 29, 31, and 32 also give good results, while the application of MW-MCC to the remaining emissive bands, and to lower frequency bands, like 19 or below, produces very few vectors. This is due to the fact that the patterns produced are not well-defined, in particular far from the coast. Probably some non-linear scaling of the brightness during image pre-processing could improve the results. Work on this is also in progress.

The differences between daytime and night time have been discussed in the paper. It has been observed that factors related to thermal exchanges in the water column affect the MW-MCC results. In particular, lower temperature variations during the night allow a better pattern tracking, with an increase in the number of current vectors of around 30% for bands 22, 23, and 65% for band 20.

Some examples of current flows obtained by MW-MCC, and the case study of a comparison between HF radar measurements and MW-MCC currents have also been shown. A strong similarity has been found between the currents computed by MW-MCC, and some well-known current flows in particular areas. Moreover, a good agreement between HF radar data or hydrodynamic model simulations and MW-MCC results has been obtained. A more systematic validation of the MW-MCC results will be done in the near future, based on data in the Tuscan Archipelago that will be obtained by a recently installed HF radar system. Furthermore, work on t he application of MW-MCC to images at a resolution of 750 m, and 375 m, coming from the latest VIIRS sensor, is in progress.

Lastly, it should be pointed out that further improvements of the pre-processing phase, like other more advanced destriping algorithms and filtering techniques, and a non-linear scaling of the image brightness in some spectral channels, are possible, in order to discard fewer satellite images, and obtain more numerous, and reliable current vectors.

## Conflict of Interest

No conflict of interest was reported by all authors.

## Acknowledgements and Funding

We wish to thank our colleagues at LaMMA Consortium for their contribution to this work: A. Ortolani for constructive discussion on the MW-MCC algorithm and C. Lapucci for assistance on chlorophyll data interpretation.

## References

Al-Amri S S, Kalyankar N V and Khamitkar S D. (2010). A comparative study of removal noise from remote sensing image. *International Journal of Computer Science*, 7(1): 32–36.

Alexanin A I, Katamanov S N and Epstein Yu S. (2005). Problems of accurate automatic navigation of NOAA/AVHRR and FY-1D satellite images: *Proceedings, 31st International Symposium on Remote Sensing of Environment: Global Monitoring for Sustainability and Security*, June: 20–24.

Algazi V R and Ford G E. (1981). Radiometric equalization of nonperiodic striping in satellite data, *Computer Graphics and Image Processing*, 16 (3):287–295 https://dx.doi/10.1016/0146-664X(81)90041-1.

Antonelli P, di Bisceglie M and Episcopo R. (2004). Destriping MODIS data using IFOV overlapping, *Geoscience and Remote Sensing Symposium, IGARSS '04. Proceedings IEEE International*, 7. https://dx.doi/10.1109/IGARSS.2004.1370171.

Barton I J. (2002). Ocean currents from successive satellite images: The reciprocal filtering technique. *Journal of Atmospheric and Oceanic Technology*, 19: 1677–1689. https://dx.doi.org/10.1175/1520-0426(2002)019<1677:OCFSSI>2.0.CO;2.

Bouali M. (2010). A simple and robust destriping algorithm for imaging spectrometers: application to MODIS data, *ASPRS 2010 Annual Conference San Diego*.

Bowen M M, Emery W J, Wilkin J L *et al.* (2002). Extracting multiyear surface currents from sequential thermal imagery using the maximum cross-correlation technique. *Journal of Atmospheric and Oceanic Technology*, 19 (10): 1665–1676. https://dx.doi.org/10.1175/1520-0426(2002)019<1665:EMSCFS>2.0.CO;2.

Breaker L C, Krasnopolsky V M, Rao D B *et al.* (1994). The feasibility of estimating ocean surface currents on an operational basis using satellite feature tracking methods. *Bulletin of American Meteorological Society*, 75: 2085–2094. https://dx.doi.org/10.1175/1520-0477(1994)075<2085:TFOEOS>2.0.CO;2.

Carvalho Jr O A, Correia da Silva N, Ferreira de Carvalho A P *et al.* (2012). Combining noise-adjusted principal components transform and median filter techniques for denoising MODIS temporal signatures. *Revista Brasileira de Geofisica*, 30(2): 147–157. https://dx.doi.org/10.1590/rbgf.v30i2.88.

Chen J, Shao Y, Guo H *et al.* (2003). Destriping CMODIS data by power filtering. *IEEE Transactions On Geoscience*

*and Remote Sensing*, 41(9): 2119–2124. https://dx.doi.org/10.1109/TGRS.2003.817206.

Crippen R E . (1989). A simple spatial filtering routine for the cosmetic removal of scan line noise from Landsat TM P-tape imagery. *Photogrammetric Engineering & Remote Sensing*, 55(3): 327–331.

Crocker R I, Emery W J, Matthews D K *et al.* (2007). Computing coastal ocean surface currents from infrared and ocean color satellite imagery. *IEEE Transactions On Geoscience and Remote Sensing*, 45(2): 435–447. https://dx.doi.org/10.1109/TGRS.2006.883461.

Di Bisceglie M, Episcopo R, Galdi C *et al.* (2009). Destriping MODIS data using overlapping field-of-view method. *IEEE Transactions On Geoscience and Remote Sensing*, 47(2): 637–651. https://dx.doi.org/10.1109/TGRS.2008.2004034.

Doronzo B, Taddei S, Brandini C *et al.* (2015). Extensive analysis of potentialities and limitations of a maximum cross-correlation technique for surface circulation by using realistic ocean model simulations. *Ocean Dynamics*, 65(8): 1183–1198. https://dx.doi.org/10.1007/s10236-015-0859-1.

Emery W J, Thomas A C, Collins M J *et al.* (1986). An objective method for computing advective surface velocities from sequential infrared satellite images. *Journal of Geophysics Research*, 91(C11): 12865–12878. https://dx.doi.org/10.1029/JC091iC11p12865.

Emery W J, Baldwin D and Matthews D K. (2003). Maximum cross correlation automatic satellite image navigation and attitude corrections for open ocean image navigation, IEEE Trans. Geosci. Remote Sens. 41: 33–42. http://dx.doi.org/10.1109/TGRS.2002.808061.

Esaias W E, Abbott M A, Barton I *et al.* (1998). An overview of MODIS capabilities for ocean science observations. *IEEE Transactions On Geoscience and Remote Sensing*, 36: 1250–1265. https://dx.doi.org/10.1109/36.701076.

Garcia C A E and Robinson I S. (1989). Sea surface velocities in shallow seas extracted from sequential Coastal Zone Color Scanner satellite data. *Journal of Geophysics Research*, 94: 12681–12691. https://dx.doi.org/10.1029/JC094iC09p12681.

Gonzales R C and Woods R E. (2002). Digital Image Processing, Prentice Hall.

Gumley L, Frey R and Moeller C. (2005). Destriping of MODIS L1B 1KM Data for Collection 5 Atmosphere Algorithms, MODIS Meetings - Poster Session. Retrieved from https://modis.gsfc.nasa.gov/sci_team/meetings/200503/posters/atmos/gumley1.pdf

Gumley L. (2002). Proceedings MODIS Workshop, *URL: Western Autralian Satellite Technology and Applications Consortium*. Nov. 26–29. Retrieved from http://www.wastac.wa.gov.au/modis_workshop_2002/Lecture_3_Scanner_Characteristics_Image_Artifacts_Destriping.ppt

Horn B K P and Woodham R J. (1979). Destriping Landsat MSS images by histogram modification. *Computer Graphics and Image Processing*, 10: 69–83. https://dx.doi.org/10.1016/0146-664X(79)90035-2.

Huang H L, Gumley L E, Strabala K *et al.* (2004). International MODIS and AIRS Processing Package (IMAPP): A Direct Broadcast Software Package for the NASA Earth Observing System. *Bulletin of the American Meteorological Society*, 85: 159–161. https://dx.doi.org/10.1175/BAMS-85-2-159.

Istituto Idrografico della Marina. (1982). Atlante delle correnti superficiali dei mari italiani, Istituto Idrografico della Marina, Genova.

Justice C O, Townshend J R G, Vermote E F *et al.* (2002). An overview of MODIS land data processing and product status. *Remote Sensing of Environment*, 83: 3–15. https://dx.doi.org/10.1016/S0034-4257(02)00084-6.

Kamachi M. (1989). Advective surface velocities derived from sequential images for rotational flow field: Limitations and applications of Maximum Cross Correlation method with rotational registration. *Journal of Geophysical Research*, 94(C12): 18227–18233. https://dx.doi.org/10.1029/JC094iC12p18227.

Kay S, Hedley J D and Lavender S. (2009). Sun glint correction of high and low spatial resolution images of aquatic scenes: A review of methods for visible and near-infrared wavelengths. *Remote Sensing*, 1(4): 697–730. https://dx.doi.org/10.3390/rs1040697.

Marcello J, Eugenio F, Marqués F *et al.* (2008). Motion estimation techniques to automatically track oceanographic thermal structures in multisensor image sequences. *IEEE Transactions On Geoscience and Remote Sensing*, 46(9): 2743–2762. https://dx.doi.org/10.1109/TGRS.2008.919274.

Matthews D K and Emery W J. (2009). Velocity observations of the California Current derived from satellite imagery. *Journal of Geophysics Research*, 114(C8). https://dx.doi.org/10.1029/2008JC005029..

Mikelsons K, Wang M, Jiang L *et al.* (2014). Destriping algorithm for improved satellite-derived ocean color product imagery. *Optics Express*, 22(23): 28058–28070. https://dx.doi.org/10.1364/OE.22.028058.

Millot C. (1999). Circulation in the Western Mediterranean Sea. *Journal of Marine Systems*, 20(1–4): 423–442. https://dx.doi.org/10.1016/S0924-7963(98)00078-5.

Minnett P J and Barton I J. (2009). Remote sensing of the earth's surface temperature, In Radiometric Temperature Measurements II. Applications. In Z M Zhang, B K Tsai, and G Machin (Eds), *Experimental Methods in the Physi-*

*cal Sciences*, vol.43, Academic Press/Elsevier, 333–391.

Notarstefano G, Poulain P and Mauri E. (2008). Estimation of surface currents in the Adriatic Sea from sequential infrared satellite images. *Journal of Atmospheric and Oceanographic Technology*, 25: 271–285. https://dx.doi.org/10.1175/2007JTECHO527.1.

Pan J J and Chang C I. (1992). Destriping of Landsat MSS images by filtering techniques, *Photogrammetric Engineering & Remote Sensing,* 58(10): 1417–1423.

Prasad J S, Reajawat A S, Pradhan Y *et al.* (2002). Retrieval of sea surface velocities using sequential ocean color monitor data. *Proceedings of Indian Academy of Sciences, Earth and Planetary Sciences,* 111(3): 189–195. http://dx.doi.org/10.1007/BF02701965.

Rainey K and Hallenborg E. (2013). Characterization of Sun Glitter Statistics in Ocean Video, SSC Pacific, San Diego, CA, Tech. Rep. 2031.

Rakwatin P, Takeuchi W and Yasuoka Y. (2007). Stripe noise reduction in MODIS data by combining histogram matching with facet filter. *IEEE Transactions On Geoscience and Remote Sensing,* 45(6): 1844–1856. http://doi.org/10.1109/TGRS.2007.895841.

Schroeder K. Haza A C, Griffa A *et al.* (2011). Relative dispersion in the Liguro-Provencal basin: From sub-mesoscale to mesoscale. *Deep Sea Research Part I: Oceanographic Research Papers*, 58: 209–228. https://dx.doi.org/10.1016/j.dsr.2010.11.004.

Shao Y, Taff G N and Lunetta R S. (2011). A review of selected moderate-resolution imaging spectroradiometer algorithms, data products, and applications. In: Q. Weng (ed.), *Advances in Remote Sensing* — Chapter 2: 31–55. Boca Raton, Florida: CRC Press LLC. https://dx.doi.org/10.1201/b10599-4.

Shchepetkin A F and McWilliams J C. (2005). The Regional Ocean Modeling System: A split-explicit, free-surface, topography following coordinates ocean model. *Ocean Modelling*, 9(4): 347–404. https://dx.doi.org/10.1016/j.ocemod.2004.08.002.

Simpson J J and Yhann S R. (1994). Reduction of noise in AVHRR channel 3 data with minimum distortion. *IEEE Transactions On Geoscience and Remote Sensing*, 32 (2): 315–328. https://dx.doi.org/10.1109/36.295047.

Simpson J J, Gobat J I a nd Frouin R. (1995). Improved destriping of GOES images using finite impulse response filters. *Remote Sensing of Environment*, 52(1): 15–35. https://dx.doi.org/10.1016/0034-4257(94)00078-2.

Simpson J J, Stitt J R and Leath D M. (1998). Improved finite impulse response filters for enhanced destriping of geostationary satellite data. R*emote Sensing of Environment*, 66(3): 235–249. https://dx.doi.org/10.1016/S0034-4257(98)00070-4.

Srinivasan R, Cannon M and White J. (1988). Landsat data destriping using power spectral filtering, *Optical Engineering*, 27(11): 939–943. https://dx.doi.org/10.1117/12.7976791.

Wahl D D and Simpson J J. (1990). Physical processes affecting the objective determination of near-surface velocity from satellite data. *Journal of Geophysical Research*, 95: 13511–13619. https://dx.doi.org/10.1029/JC095iC08p13511.

Weinreb M P, Xie R, Lienesch J H *et al.* (1989). Destriping GOES images by matching empirical distribution functions. *Remote Sensing of Environment*, 29(2): 185–195. https://dx.doi.org/10.1016/0034-4257(89)90026-6.

Zavialov P O, Grigorieva J V, Moller O O Jr *et al.* (2002). Continuity preserving modified maximum cross-correlation technique. Journal of Geophysical Research, 94 (C10): 24-1–24-10. https://dx.doi.org/10.1029/2001JC001116.